Transport and Communications Science Journal, Vol. 76, Issue 07 (09/2025), 1010-1022

Transport and Communications Science Journal

FRACTURE RESPONSE OF CONCRETE CONTAINING CARBON NANOTUBES UNDER VARIOUS LOADING CONDITIONS

Dang Van Phi[1,2*], Pham Duc Tho[1,2], Nguyen Manh Tuan[3]

[1]Hanoi University of Mining and Geology, No18 Pho Vien Street, Hanoi, Vietnam

[2]GECS Research group, Hanoi University of Mining and Geology, No18 Pho Vien Street, Hanoi, Vietnam

[3]Party Committee of Khanh Khe commune, Binh Trung village, Khanh Khe commune, Lang Son province, Vietnam

ARTICLE INFO

TYPE: Research Article
Received: 16/05/2025
Revised: 07/08/2025
Accepted: 10/09/2025
Published online: 15/09/2025
https://doi.org/10.47869/tcsj.76.7.7
* *Corresponding author*
Email: dangvanphi@humg.edu.vn; Tel: +84828316888

Abstract: The demand for high-performance cementitious materials capable of sustaining extreme mechanical loads has intensified in recent years, as conventional concrete often suffers from brittle fracture and limited durability under dynamic actions. Nanomaterials such as carbon nanotubes (CNTs) have emerged as promising additives owing to their remarkable mechanical and interfacial properties, offering the potential to enhance the fracture resistance of ultra-high-performance fiber-reinforced concretes (UHPFRCs). This study explores the fracture durability of UHPFRCs incorporating CNTs under both static and impact loading conditions. Mixtures were prepared with CNT dosages ranging from 0% to 1.5% by cement weight, and fracture behavior was evaluated through fracture strength (f_t), specific work of fracture (W_S), total fracture energy (W_E), and softening fracture energy (W_F). The experimental results indicated that CNT addition substantially improved fracture resistance, particularly tensile strength, across all loading rates. The mixture containing 1.0% CNTs achieved the highest fracture strength and exhibited the maximum dynamic increase factor (DIF) compared with the control and other CNT dosages. Furthermore, fracture parameters f_t, W_S, and W_E demonstrated pronounced sensitivity to loading rate, with DIF values ranging from 1.21 to 4.50, while W_F remained nearly unchanged, with DIF values between 0.90 and 0.98. These outcomes confirm that CNTs strengthen the fiber–matrix interfacial zone, leading to more efficient stress transfer and improved durability. The findings provide valuable insights for the design of UHPFRCs with superior performance under both static and impact loads, contributing to the development of resilient structural materials.

Keywords: Fracture characteristics, carbon nanotubes, impact loading, dynamic increase factors.

1. INTRODUCTION

The structural response to high-rate loading is significantly influenced by the ability to absorb energy prior to collapse. Enhancing this energy absorption capacity represents a practical strategy to improve safety and mitigate catastrophic failures in infrastructure subjected to extreme loading conditions [1]. Previous studies have been proposed to improve the energy dissipation performance of concrete, such as incorporating deformed steel fibers, employing hybrid fiber systems combining different types of steel or a mix of steel and polyamide fibers, and optimizing the particle size distribution of the granular constituents [2–5].

Although the fracture resistance and energy dissipation performance of concrete have been investigated with different materials, there is a notable absence of published research on UHPFRCs containing nanoparticles (NPs). According to Ruan et al. [6], incorporating nano-zirconia at a dosage of 3 wt.% significantly enhanced the fracture energy of reinforced reactive powder concrete (RPC), with an 85.7% improvement observed during four-point bending tests relative to RPC without NZ. Gdoutos et al. [7] conducted research on the fracture durability of mortar reinforced with carbon nanofibers and carbon nanotubes (CNTs) under static loads. Their findings revealed that incorporating 0.1 % CNTs enhanced the flexural strength by 86.7% and the fracture toughness by 85.7%. Stynoski et al. [8] found that incorporating CNTs into mortar led to an improvement of 5-10% in bending performance and resistance to crack propagation. According to Maio et al. [9], the addition of graphite to concrete enhanced its fracture energy during quasi-static loading, with the enhancement from 2.8 kJ/m² to 3.8 kJ/m² corresponding to a graphite volume fraction increment from 0.05% to 0.1%. There is limited data on the effectiveness of CNTs in improving the fracture response of UHPFRCs under both static and impact loads. Existing studies have focused on improving mechanical behaviors, including tension, bond interface, compression, and flexure by incorporating different NPs [10–14]. Recently, Dang and Kim demonstrated that incorporating different NPs, including nano-$CaCO_3$, multiwalled carbon nanotubes, and nano-SiO_2, into UHPFRCs notably improved their ability to absorb mechanical energy [10]. Their results revealed that the inclusion of NPs into concrete could increase the fracture toughness of the cementitious matrix. However, the exact role of CNTs contents in improving fracture resistance at impact loads remains uncertain.

Thus, this study examines the effects of CNTs contents on the fracture response of UHPFRCs at both static and dynamic loading conditions. The addition of CNTs in UHPFRCs is expected to enhance their fracture resistance by strengthening the bonding performance of steel fibers within the matrix. This study aims to achieve the following goals: (1) to assess the effects of CNTs contents on the fracture response of UHPFRCs, (2) to examine the effect of load velocities on the fracture durability of UHPFRCs incorporating CNTs.

2. EXPERIMENTAL ANALYSES

2.1. Preparing Materials and Specimens

Tables 1 and 2 summarize the features of matrices and steel fibers, respectively [15]. The average particle size of cement was measured as 9.0 μm. Silica fume (98.5% SiO_2) and silica powder exhibited average particle sizes of 23.0 μm and 5.0 μm, respectively. CNTs were characterized by measuring approximately 10 μm in length and 200 nm in diameter. Polycarboxylate ether superplasticizer (SP) with 30% solid content was utilized to enhance

the flow capacity of matrices. The mixtures prepared included UHPFRCs without CNTs (C00), and those containing 0.5% CNTs (C05), 1.0% CNTs (C10), and 1.5% CNTs (C15).

Table 1. Weight ratio-based matrix composition and compressive strength.

Matrix	Cement	CNT	Silica sand	Silica fume	Silica powder	SP	W/C	Compressive strength (MPa)	Flow test (mm)
C00	1.00	–	1.1	0.25	0.3	0.075	0.2	186.8	220
C05	0.995	0.005	1.1	0.25	0.3	0.075	0.2	201.4	175
C10	0.99	0.010	1.1	0.25	0.3	0.075	0.2	206.2	170
C15	0.985	0.015	1.1	0.25	0.3	0.075	0.2	188.9	160

Table 2. Features of smooth steel fibers [15].

Diameter (mm)	Length (mm)	Density (g/cm^3)	Tensile strength (MPa)	Modulus (GPa)
0.3	30	7.9	2447	200

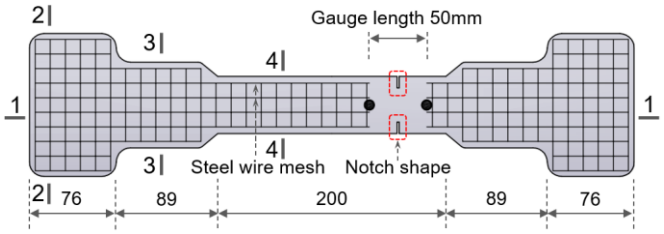

a) Static tensile specimen

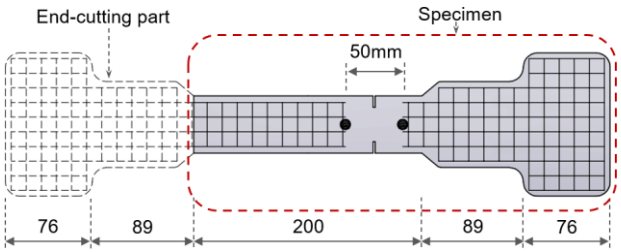

b) Impact tensile specimen

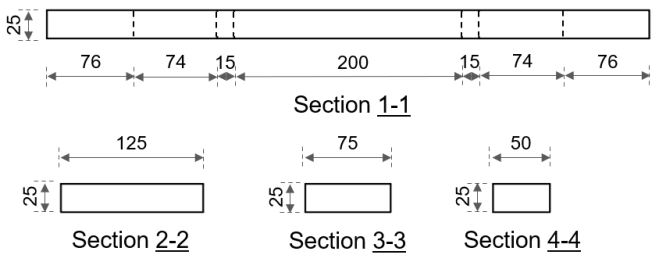

c) Cross-sections of specimens

Figure 1. Specimen geometry (unit: mm) [16].

The preparation of mixtures containing CNTs followed these steps [17]: (1) CNTs were

dispersed in a water-based solution incorporating 50% of the SP; (2) the dry components, including sand, silica fume, silica powder, and cement, were thoroughly mixed for approximately 5 minutes to ensure uniform distribution; (3) the solution containing water, CNTs, and SP was gradually introduced into the mixture over 2 minutes; (4) the rest of the SP was gradually introduced and blended for 5 minutes. Steel fibers were ultimately added by hand in mixtures and further blended for an additional 2 minutes. The specimens were kept at a temperature of 20 ± 2 °C for 48 hours before being demolded. Subsequently, they were immersed in hot water maintained at 90 ± 2 °C for 72 hours. All tests were conducted after a curing period of 28 days.

Figure 1 depicts the dimensions and shapes of the specimens adopted for static and impact loading conditions. To ensure accurate measurement of fracture parameters, two layers of steel wire mesh were embedded in the specimens to limit crack propagation beyond the gauge length [18]. For the preparation of impact test specimens, the bell-shaped end section of the static sample was cut off, and a longer segment of the wire mesh was attached to the transmitter bar.

2.2. Setup and procedure for testing

Figure 2 illustrates the universal testing machine (UTM) utilized to perform static tensile tests under a constant velocity of 1.0 mm/min. To measure elongation along the gauge length, two linear variable differential transformers (LVDTs) were linked to the samples during testing, and a load cell placed above the specimens within the machine measured the tensile stresses.

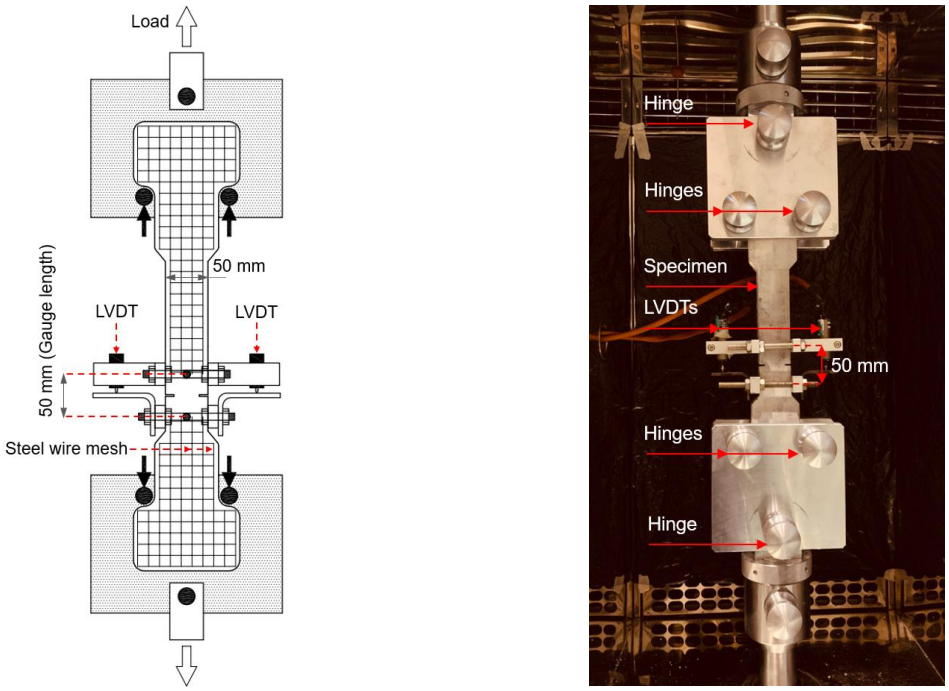

Figure 2. Setup of specimens and equipment in static conditions [16].

Figure 3 provides a detailed depiction of the setup used for conducting the dynamic tensile tests, as outlined in references [10,18–21]. A coupling device was utilized to attach the two energy frames to the pullout bar of the hydraulic jack system, as illustrated in Fig. 3. The

sample was positioned between the energy frames, with one end secured to a hinged connector and the opposite end fastened to a transmitter bar anchored by a rigid support [18,21].

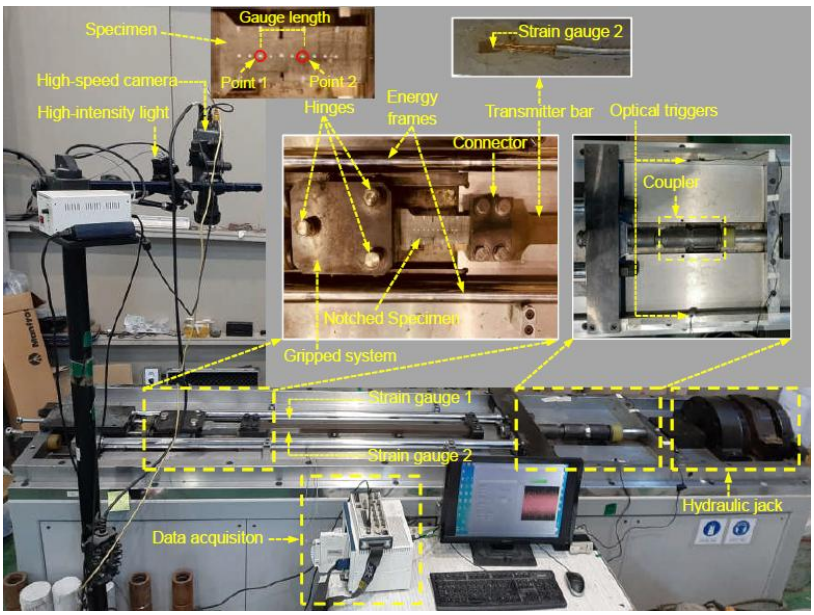

Figure 3. Experimental setup for tensile impact tests [10].

A 1960 kN-capacity coupler was used to ensure reliable load transfer during the testing process. Once the coupler reached its load-bearing limit under the hydraulic jack system, its rupture triggered the rapid release of elastic strain energy from the two energy frames, initiating a propagating stress wave [18,21]. Furthermore, a high-speed camera was employed during the tensile impact testing to evaluate the elongation of the samples, analyzing a series of sequential images capturing the behavior at points 1 and 2, as shown in Fig. 3. Besides, the tensile stress was determined by two strain gauges located on the transmitter bars.

The tensile stress-strain characteristics of the matrices under impact conditions were evaluated through the steps described in [20]: (1) to determine the velocity profiles of points 1 and 2 located on the specimen surface by processing sequential images captured with a high-speed camera system (Fig. 4a); (2) using the velocity histories derived from high-speed imagery, determine and plot the temporal evolution of tensile strain in the specimen; (3) to evaluate the strain-time profile of the specimen to determine the point associated with the transition to high strain rate conditions (Fig. 4b); (4) to obtain the stress history of the specimen, the signals measured by two strain gauges on opposite sides of the transmitter bar were utilized; (5) to identify the initial time point in the stress-time history as well as the corresponding event time, as shown in Fig. 4c; and (6) to generate the tensile stress-strain curve by aligning the strain and stress histories in time, as shown in Fig. 4d.

The impact velocity depends on the wave speed (C) and the strain (ε_f) of the energy frame at coupler failure as described in Eq. (1), whereas the strain rate (ε') is determined from the velocities at points 1 and 2 (v_1, v_2), measured across a gauge length (GL), as defined in Eq. (2) [20].

$$V = C.\varepsilon_f \tag{1}$$

$$\varepsilon' = \frac{v_2 - v_1}{GL} \tag{2}$$

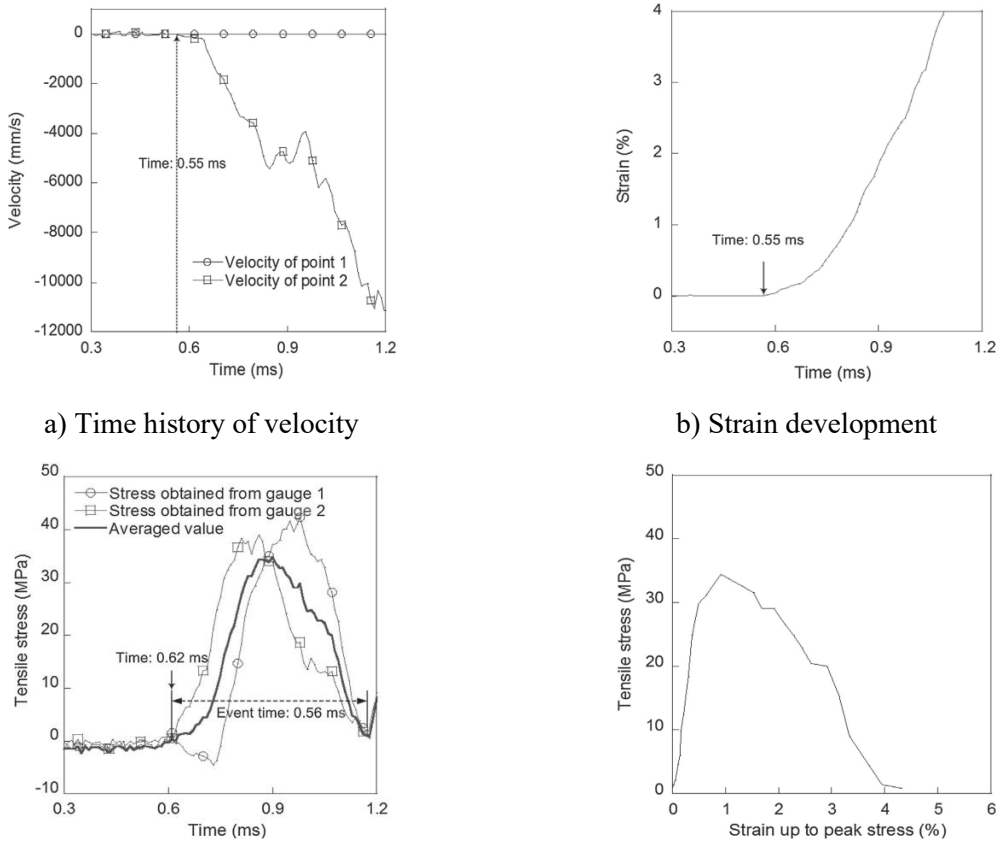

a) Time history of velocity

b) Strain development

c) Stress response

d) Stress–strain response

Figure 4. Experimental results under dynamic loading conditions [20].

3. RESULTS AND DISCUSSION

3.1. Fracture behavior of UHPFRCs

Figure 5 provides the fracture parameters used to evaluate the fracture resistance of UHPFRCs [3]: the fracture strength (f_t) refers to the peak tensile stress observed during the loading process before failure occurs; the specific work-of-fracture (W_S) corresponds to the energy absorbed before peak stress, calculated as the area under the tensile stress-displacement curve up to the maximum load. The softening fracture energy (W_F), representing the softening fracture energy in the post-peak region, reflects the energy dissipated during crack propagation; the total fracture energy (W_E) corresponds to the area under the entire load-displacement curve, while the displacement capacity (δ_c) refers to the displacement at the tensile strength at f_t.

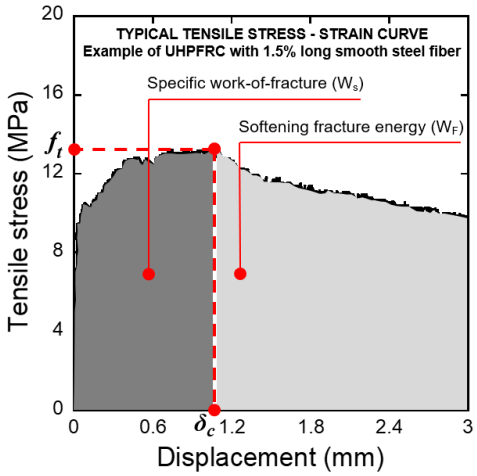

Figure 5. Characteristic tensile behavior and fracture properties of UHPFRCs [16].

3.2. Influence of CNTs on the fracture characteristics of UHPFRCs

Table 3 summarizes the fracture responses of matrices subjected to static and impact loading conditions. The fracture resistance of UHPFRCs was influenced by CNTs content, as matrices with CNTs exhibited higher tensile parameters compared to the control (C00).

Table 3. Fracture responses of samples subjected to static and impact conditions.

Matrix	Load	f_t		δ_c		W_S		W_F		W_E	
		MPa	DIF	mm	DIF	kJ/m²	DIF	kJ/m²	DIF	kJ/m²	DIF
C00	Static	14.72	1.00	0.437	1.00	5.55	1.00	28.44	1.00	33.99	1.00
	Impact	29.31	1.99	1.003	2.30	25.00	4.50	26.61	0.94	51.61	1.52
C05	Static	15.45	1.00	0.456	1.00	6.29	1.00	35.66	1.00	41.95	1.00
	Impact	31.95	2.07	0.859	1.88	19.51	3.10	34.92	0.98	57.42	1.30
C10	Static	16.04	1.00	0.475	1.00	6.94	1.00	40.82	1.00	47.76	1.00
	Impact	34.00	2.12	0.905	1.91	21.48	3.10	36.54	0.90	58.02	1.21
C15	Static	14.86	1.00	0.440	1.00	5.71	1.00	33.16	1.00	38.87	1.00
	Impact	30.19	2.03	0.971	2.21	22.03	3.86	30.40	0.92	52.43	1.35

Under static loading, f_t values of the C00, C05, C10, and C15 matrices were 14.72, 15.45, 16.04, and 14.86 MPa, respectively, whereas under impact loading, the corresponding values were 29.31, 31.95, 34.00, and 30.19 MPa, as detailed in Table 3. The presence of CNTs contributes to a stronger matrix-fiber interface, which in turn promotes superior tensile behavior in UHPFRCs [10,22]. The f_t value for the C00 matrix obtained in this study was

consistent with the value of 14.8 MPa reported by Tran et al. [3] for UHPFRC under similar static loading conditions.

The W_S values of the C05, C10, and C15 matrices under impact loading were generally lower than those of the C00 matrix under static loading, whereas under static loading, their W_S values exceeded those of the C00 matrix. The W_S values of the C00, C05, C10, and C15 matrices at impact loads were 25.00, 19.51, 21.48, and 22.03 kJ/m^2, respectively, whereas their values at static loads were 5.55, 6.29, 6.94, and 5.71 kJ/m^2, respectively (Table 3). However, the W_F of all samples exhibited a slight reduction under impact loads, in contrast to the W_F observed under static loading conditions. For instance, the W_F of C00 at static velocity was 28.44 kJ/m², but it decreased to 26.61 kJ/m² under impact velocity (Table 3). The decrease in the W_F values is addressed in more detail in Section 3.3.

Figures 6 and 7 illustrate a comparison of typical crack patterns observed in matrices with CNTs (C10) and without CNTs (C00). Across both quasi-static and impact loading conditions, the C10 matrix exhibited narrower crack openings compared to the C00 matrix, despite the presence of fiber bridging in both matrices. The observed improvement can be linked to the reinforcing effect of CNTs on both the matrix interface and its compressive integrity [3,16,23].

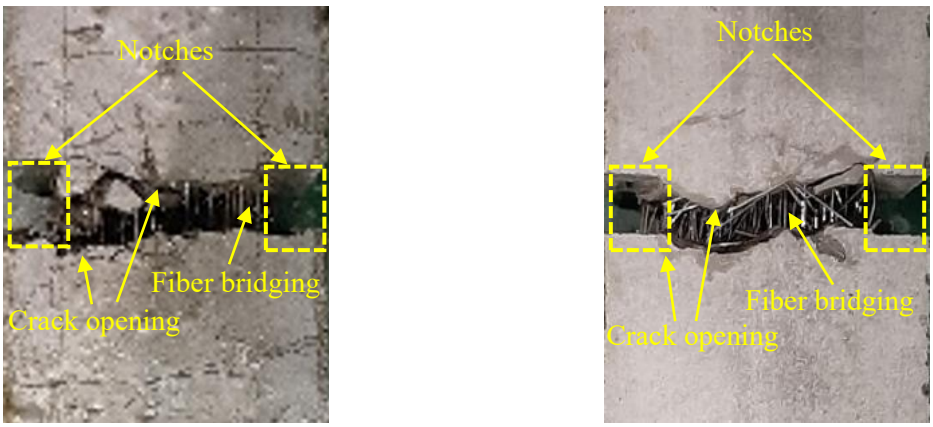

a) C00 b) C10

Figure 6. Comparison of typical crack patterns observed in C00 and C10 at static loads.

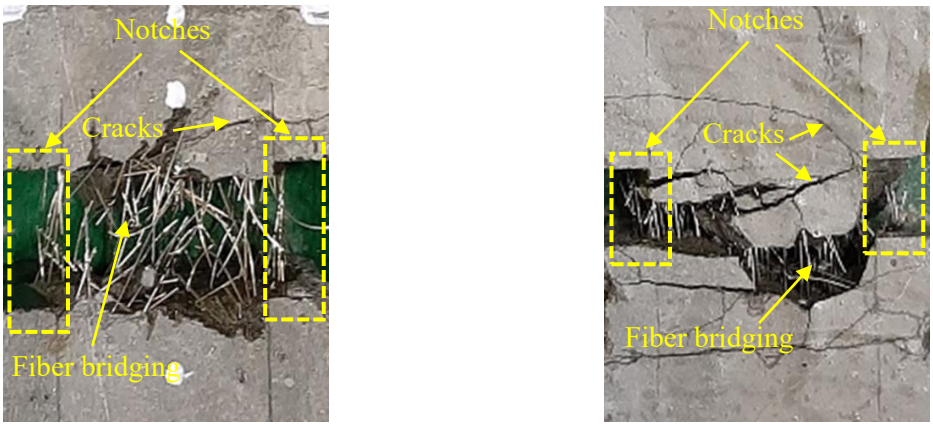

a) C00 b) C10

Figure 7. Comparison of typical crack patterns observed in C00 and C10 at impact loads.

3.3. Influence of loading velocity on the fracture behavior of UHPFRCs

This study utilizes the dynamic increase factor (DIF) to evaluate changes in key mechanical parameters (f_t, W_S, W_F, W_E, and δ_c) resulting from elevated loading rates compared to quasi-static loading. The DIF represents a dimensionless metric that characterizes the rate sensitivity of a material subjected to different loading velocities or strain rates, as described in Eq. (3) [24].

$$DIF = \frac{\Delta_i}{\Delta_j} \tag{3}$$

where Δ_i is the response at a dynamic loading rate, and Δ_j corresponds to that under quasi-static conditions.

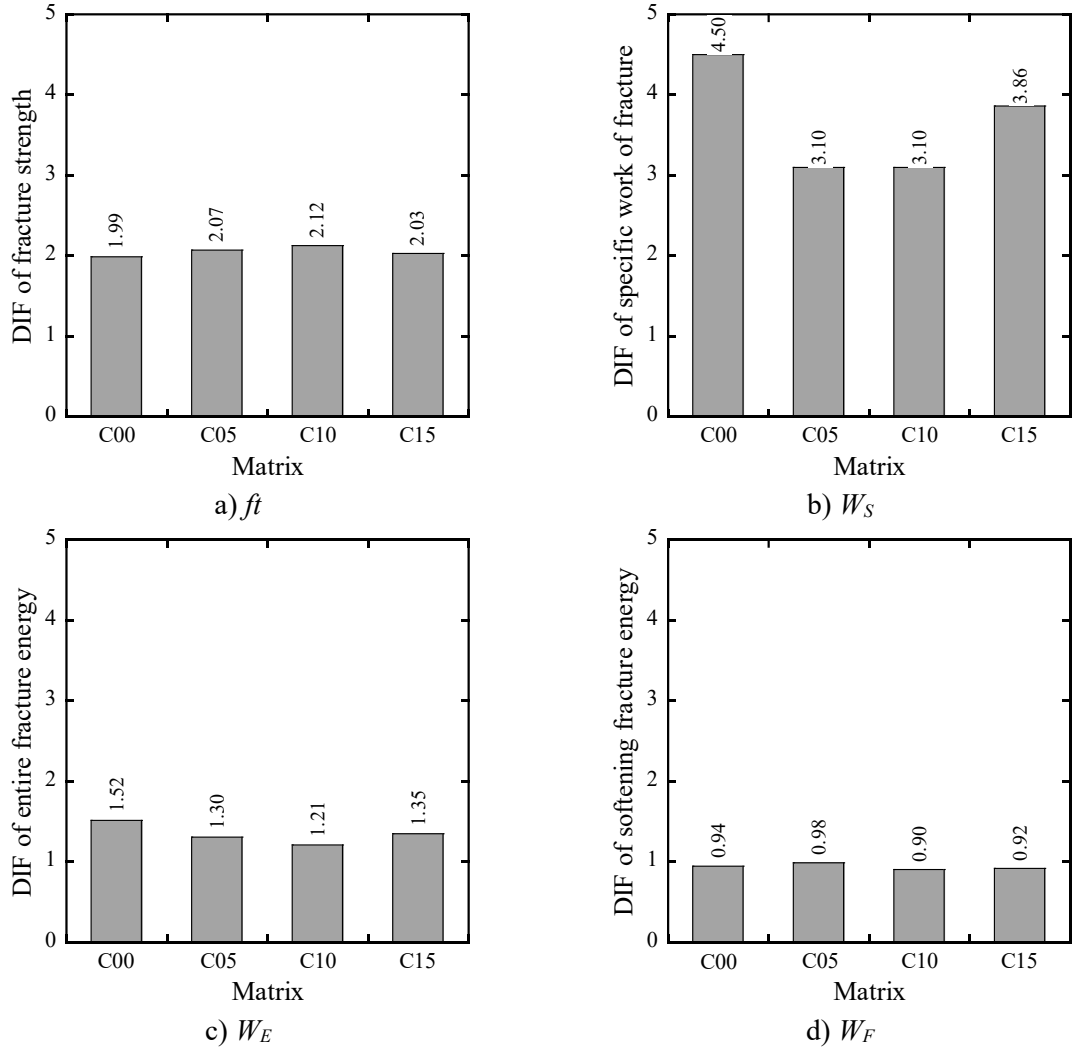

Figure 8. Sensitivity of UHPFRC fracture properties to loading.

Figure 8 depicts the DIF values corresponding to the fracture-related properties of matrices. The f_t, W_S, and W_E revealed strong sensitivity to changes in loading velocity under static and impact conditions, whereas W_F displayed no noticeable sensitivity. The DIFs for the f_t of the C00, C05, C10, and C15 matrices were 1.99, 2.07, 2.12, and 2.03, respectively, while

the corresponding DIFs associated with W_S were 4.50, 3.10, 3.10, and 3.86, respectively, as shown in Figs. 8a-b. Besides, the DIF values for the W_E were recorded as 1.52, 1.30, 1.21, and 1.35 for the C00, C05, C10, and C15 matrices, respectively, as presented in Fig. 8c. At high strain rates, the fracture resistance of the matrices is influenced by the quality of adhesion at the fiber-matrix interface [10]. Additionally, UHPFRCs containing CNTs exhibited greater fracture resistance compared to C00, resulting from the improved dispersion and packing density of CNTs within the matrices and fiber matrix zones around the smooth steel fibers, which substantially enhanced the interfacial bond strength of the embedded fibers [10].

In contrast, the DIF for the W_F demonstrated an insensitivity to strain rate variations in all matrices. The DIF values for the W_F of C00, C05, C10, and C15 were 0.94, 0.98, 0.90, and 0.92, respectively, as depicted in Fig. 8d. A declining trend in W_F values under higher strain rates agrees with results documented in earlier studies [3]. The reduction in W_F at higher load velocity may result from the accelerated degradation of tensile response beyond the f_t point [3]. Moreover, the rate-dependent behavior of W_F is strongly influenced by the pullout resistance sensitivity to loading velocity, which is predominantly governed by the interfacial friction between steel fibers and the surrounding matrix; however, the friction exhibits a pronounced sensitivity to load changes [20]. Consequently, the loading-rate sensitivity of UHPFRCs in tension was predominantly attributed to the interfacial bond capacity of smooth steel fibers, leading to enhanced fracture resistance at high loading velocity [10,25].

3.4. Influence of CNTs on compressive strength and flowability of UHPFRCs

A marked increase in the compressive strength of matrices was observed with the inclusion of CNTs, as compared to the reference matrix mixture (C00 without CNTs), as provided in Table 1. The C05, C10, and C15 matrices exhibited compressive strengths of 201.4, 206.2, and 188.9 MPa, respectively, compared to 186.8 MPa for the C00 matrix. The compressive strength of the matrices containing CNTs slightly declined when the CNTs content exceeded 1.0%. The decrease in compressive strength observed in the C15 matrix could be attributed to the formation of CNT agglomerates at high dosages, as suggested by Wu et al. [22].

In addition, all matrices containing CNTs had flowability values less than 175 mm, which were lower than the 220 mm observed for the C00 matrix without CNTs (Table 1). Moreover, an increase in the CNTs content of the matrices resulted in a significant decrease in their mini-slump flows. The mini-slump flow measurements for the matrices with a CNTs contents of 0.5%, 1.0%, and 1.5% were 175, 170, and 160 mm, respectively, as provided in Table 1. This can be attributed to the fact that incorporating CNTs significantly raises the water requirement of the mixtures [26,27]. The water demand of cementitious materials is predominantly governed by the volume required to fill the interparticle voids and the quantity adsorbed onto the surfaces of the solid constituents [26].

4. CONCLUSIONS

In this study, the influence of different CNTs contents on the fracture behavior of UHPFRCs was examined. Three various dosages of CNTs, including 0.5%, 1.0%, and 1.5% were considered. In addition, the fracture durability of the UHPFRCs was evaluated under both static and impact loads. The main conclusions drawn from the experimental results are as follows:

- The incorporation of CNTs into UHPFRCs significantly enhances their fracture resistance, as evidenced by improved tensile properties under both static and impact-loading conditions. The matrices with CNTs exhibited higher fracture strength compared to the control matrix, with the 1% CNTs content achieving the highest fracture resistance among the tested dosages in UHPFRCs.
- The load sensitivity of the fracture responses of UHPFRCs was dependent on the CNTs content, and the UHPFRC with 1.0% CNTs produced the highest DIF values for fracture strength in comparison to those of UHPFRCs containing 0.5% or 1.5% CNTs content.
- The f_t, W_S, and W_E of UHPFRCs demonstrated marked sensitivity to variations in loading velocity under static and impact conditions, whereas W_F remained largely unaffected. As the loading rate changes from static to impact conditions, the DIF values of f_t, W_S, and W_E of UHPFRCs are all greater than 1.0, ranging from 1.21 to 4.50, while the DIF values corresponding to W_F are less than 1.0, within the range of 0.90 to 0.98.
- The addition of CNTs markedly enhanced the compressive strength of UHPFRCs compared to UHPFRCs without any CNTs. However, a slight reduction in compressive strength occurred when CNTs content exceeded 1.0%, likely due to CNTs agglomeration in UHPFRCs.

The findings of this study confirm that incorporating varying concentrations of CNTs into UHPFRCs improves their fracture resistance. Despite growing interest in UHPFRCs, the influence of critical factors, including CNTs distribution, size, and specimen-dependent geometry, on their fracture behavior is not yet fully understood. To advance the current knowledge, employing high-resolution microstructural analysis techniques (e.g., SEM) is crucial for accurately characterizing CNT distribution and assessing its role in mechanical performance. Furthermore, optimizing the dosage of CNT through a more refined concentration range, including both lower (e.g., 0.1%, 0.3%) and intermediate levels (e.g., 0.75%, 1.25%), is expected to provide deeper insight into their influence on fracture characteristics. Consequently, further research is required to address these knowledge gaps.

REFERENCES

[1]. T.K. Tran, D.J. Kim, High strain rate effects on direct tensile behavior of high performance fiber reinforced cementitious composites, Cem. Concr. Compos., 45 (2014) 186–200. https://doi.org/10.1016/j.cemconcomp.2013.10.005

[2]. S. Pyo, S. El-Tawil, A.E. Naaman, Direct tensile behavior of ultra high performance fiber reinforced concrete (UHP-FRC) at high strain rates, Cem. Concr. Res., 88 (2016) 144–156. https://doi.org/10.1016/j.cemconres.2016.07.003

[3]. N.T. Tran, T.K. Tran, J.K. Jeon, J.K. Park, D.J. Kim, Fracture energy of ultra-high-performance fiber-reinforced concrete at high strain rates, Cem. Concr. Res., 79 (2016) 169–184. https://doi.org/10.1016/j.cemconres.2015.09.011

[4]. R. Yu, P. Spiesz, H.J.H. Brouwers, Static properties and impact resistance of a green ultra-high performance hybrid fibre reinforced concrete (UHPHFRC): Experiments and modeling, Constr. Build. Mater., 68 (2014) 158–171. https://doi.org/10.1016/j.conbuildmat.2014.06.033

[5]. Y. Ju, H. Liu, G. Sheng, H. Wang, Experimental study of dynamic mechanical properties of reactive powder concrete under high-strain-rate impacts, Sci. China Technol. Sci., 53 (2010) 2435–2449. https://doi.org/10.1007/s11431-010-4061-x

[6]. Y. Ruan, B. Han, X. Yu, Z. Li, J. Wang, S. Dong, J. Ou, Mechanical behaviors of nano-zirconia reinforced reactive powder concrete under compression and flexure, Constr. Build. Mater., 162 (2018) 663–673. https://doi.org/10.1016/j.conbuildmat.2017.12.063
[7]. E.E. Gdoutos, M.S. Konsta-Gdoutos, P.A. Danoglidis, Portland cement mortar nanocomposites at low carbon nanotube and carbon nanofiber content: A fracture mechanics experimental study, Cem. Concr. Compos., 70 (2016) 110–118. https://doi.org/10.1016/j.cemconcomp.2016.03.010
[8]. P. Stynoski, P. Mondal, C. Marsh, Effects of silica additives on fracture properties of carbon nanotube and carbon fiber reinforced Portland cement mortar, Cem. Concr. Compos., 55 (2015) 232–240. https://doi.org/10.1016/j.cemconcomp.2014.08.005
[9]. U. De Maio, N. Fantuzzi, F. Greco, L. Leonetti, A. Pranno, Failure analysis of ultra high-performance fiber-reinforced concrete structures enhanced with nanomaterials by using a diffuse cohesive interface approach, Nanomaterials, 10 (2020) 1–23. https://doi.org/10.3390/nano10091792
[10]. V.P. Dang, D.J. Kim, Effects of nanoparticles on the tensile behavior of ultra-high-performance fiber-reinforced concrete at high strain rates, J. Build. Eng., 63 (2023) 105513. https://doi.org/10.1016/j.jobe.2022.105513
[11]. W. Li, Z. Huang, F. Cao, Z. Sun, S.P. Shah, Effects of nano-silica and nano-limestone on flowability and mechanical properties of ultra-high-performance concrete matrix, Constr. Build. Mater., 95 (2015) 366–374. https://doi.org/10.1016/j.conbuildmat.2015.05.137
[12]. Z. Wu, K.H. Khayat, C. Shi, Effect of nano-SiO2 particles and curing time on development of bond properties and microstructure of ultra-high strength concrete, Cem. Concr. Res., 95 (2017) 247–256. https://doi.org/10.1016/j.cemconres.2017.02.031
[13]. Z. Wu, C. Shi, K.H. Khayat, Multi-scale investigation of microstructure, fiber pullout behavior, and mechanical properties of ultra-high performance concrete with nano-CaCO3 particles, Cem. Concr. Compos., 86 (2018) 255–265. https://doi.org/10.1016/j.cemconcomp.2017.11.014
[14]. K. Wille, K.J. Loh, Nanoengineering ultra-high-performance concrete with multiwalled carbon nanotubes, Transp. Res. Rec., 2142 (2010) 119–126. https://doi.org/10.3141/2142-18
[15]. V.P. Dang, D.J. Kim, Rate-sensitive pullout resistance of smooth steel fibers embedded in ultra-high-performance concrete containing nanoparticles, Concr. Cem. Concr. Compos., (2023). https://doi.org/10.1016/j.cemconcomp.2023.105109
[16]. V.P. Dang, D.J. Kim, Fracture resistance of ultra-high-performance fiber-reinforced concrete containing nanoparticles at high strain rates, Eng. Fract. Mech., 289 (2023) 109436. https://doi.org/10.1016/j.engfracmech.2023.109436
[17]. S.Y. Lee, H.V. Le, D.J. Kim, Self-stress sensing smart concrete containing fine steel slag aggregates and steel fibers under high compressive stress, Constr. Build. Mater., 220 (2019) 149–160. https://doi.org/10.1016/j.conbuildmat.2019.05.197
[18]. T.K. Tran, D.J. Kim, Investigating direct tensile behavior of high performance fiber reinforced cementitious composites at high strain rates, Cem. Concr. Res., 50 (2013) 62–73. https://doi.org/10.1016/j.cemconres.2013.03.018
[19]. N.T. Tran, T.K. Tran, D.J. Kim, High rate response of ultra-high-performance fiber-reinforced concretes under direct tension, Cem. Concr. Res., 69 (2015) 72–87. https://doi.org/10.1016/j.cemconres.2014.12.008
[20]. S.H. Park, D.J. Kim, S.W. Kim, Investigating the impact resistance of ultra-high-performance fiber-reinforced concrete using an improved strain energy impact test machine, Constr. Build. Mater., 125 (2016) 145–159. https://doi.org/10.1016/j.conbuildmat.2016.08.027
[21]. T.K. Tran, D.J. Kim, Strain energy frame impact machine (SEFIM), J. Adv. Concr. Technol., 10 (2012) 126–136. https://doi.org/10.3151/jact.10.126
[22]. Z. Wu, K.H. Khayat, C. Shi, B.F. Tutikian, Q. Chen, Mechanisms underlying the strength enhancement of UHPC modified with nano-SiO2 and nano-CaCO3, Cem. Concr. Compos., 119 (2021) 103992. https://doi.org/10.1016/j.cemconcomp.2021.103992
[23]. J.K. Park, S.W. Kim, D.J. Kim, Matrix-strength-dependent strain-rate sensitivity of strain-hardening fiber-reinforced cementitious composites under tensile impact, Compos. Struct., 162 (2017) 313–324. https://doi.org/10.1016/j.compstruct.2016.12.022

[24]. V.P. Dang, H.V. Le, D.J. Kim, Loading rate effects on the properties of fiber-matrix zone surrounding steel fibers and cement based matrix, Constr. Build. Mater., 283 (2021) 122694. https://doi.org/10.1016/j.conbuildmat.2021.122694
[25]. E. Cadoni, A. Meda, G.A. Plizzari, Tensile behaviour of FRC under high strain-rate, Mater. Struct. Constr., 42 (2009) 1283–1294. https://doi.org/10.1617/s11527-009-9527-6
[26]. H.F.W. Taylor, Cement chemistry, 2nd ed., Thomas Telford, London, 1997.
[27]. Z. Wu, C. Shi, K.H. Khayat, S. Wan, Effects of different nanomaterials on hardening and performance of ultra-high strength concrete (UHSC), Cem. Concr. Compos., 70 (2016) 24–34. https://doi.org/10.1016/j.cemconcomp.2016.03.003